Astronomy & Astrophysics manuscript no. ms
July 31, 2024

Magnetic field diagnostics of prominences with the Mg ii k line: 3D Stokes inversions vs. traditional methods

Jiří Štěpán[1], Tanausú del Pino Alemán[2, 3], and Javier Trujillo Bueno[2, 3, 4]

[1] Astronomical Institute of the Czech Academy of Sciences, Fričova 298, 25165 Ondřejov, Czech Republic
[2] Instituto de Astrofísica de Canarias, E-38205 La Laguna, Tenerife, Spain
[3] Departamento de Astrofísica, Universidad de La Laguna, E-38206 La Laguna, Tenerife, Spain
[4] Consejo Superior de Investigaciones Científicas, Spain

Received XXXX; accepted XXXX

ABSTRACT

The Mg ii k resonance line is commonly used for diagnosing the solar chromosphere. Here we theoretically investigate its intensity and polarization in solar prominences, taking into account the effects of 3D radiative transfer and the Hanle and Zeeman effects. We use an optically thick 3D model representative of a solar prominence and apply several inversion methods to the synthetic Stokes profiles, clarifying their pros and cons for inferring prominence magnetic fields. We conclude that the self-consistent 3D inversion with radiative transfer is necessary to determine the magnetic field vector, although its geometry cannot be inferred with full fidelity. We also demonstrate that more traditional methods, such as those based on the weak field approximation or the constant-property slab assumption, can offer useful information under certain conditions.

Key words. Polarization – Radiative transfer – Sun: filaments, prominences – Sun: magnetic fields

1. Introduction

Among the various spectral lines used in the diagnostic of the solar chromosphere and prominences, we have the Mg ii h and k lines, located at 280.3 nm and 279.6 nm, respectively. This ultraviolet (UV) resonance doublet is known for its strong sensitivity to the physical conditions of the plasma, making it a valuable tool for its probing.

Recently, there has been an increased interest in these UV lines thanks to the spectroscopic observations obtained by the Interface Region Imaging Spectrograph (IRIS; De Pontieu et al. 2014) and the spectropolarimetric data achieved by the two Chromospheric LAyer SpectroPolarimeter missions, CLASP2 (Narukage et al. 2016) and CLASP2.1 (McKenzie et al. 2021). These suborbital space experiments have provided unprecedented observations of the Mg ii h and k lines, confirming previous theoretical predictions, and revealing new insights into the structure and dynamics of the upper solar atmosphere (see the review by Trujillo Bueno & del Pino Alemán 2022).

Building on the success of these missions, the scientific community is now planning the Chromospheric Magnetism Explorer (CMEx) space telescope (Bryans & The CMEx Team 2023), which will focus on spectropolarimetry of the spectral region of the Mg ii h & k doublet. This new mission is expected to provide detailed information on the magnetic field and dynamics of the plasma in the chromosphere and prominences.

For the last forty years, there have been many studies with the objective of understanding the formation of the Mg ii h & k lines in prominences to explain the available prominence observations. The first two-dimensional free-standing slab models of prominences were developed by Vial (1982) using the complete frequency redistribution (CRD) approximation for calculating the Mg ii k line intensity. Later, Paletou et al. (1993) found similar results for the core of the h and k lines with both CRD and accounting for partial frequency redistribution (PRD) effects in prominences. Heinzel et al. (2014) conducted a thorough analysis using 1D prominence slab models and confirmed that the results obtained using a two-level Mg ii atomic model without continuum agrees with those using a multi-level plus continuum model. Their investigation indicated that prominences are generally optically thick in the k line, with line-center thicknesses reaching up to 10^3 or 10^4. Jejčič et al. (2018) compared 1D models with IRIS data of prominences and found that the integrated line intensities require optically thick plasma.

The magnetic field strength in quiescent solar prominences presumably ranges from a few to several tens of gauss, although it can occasionally reach significantly higher values (Hillier 2018). While in the chromosphere the h & k doublet exhibits remarkable linear polarization signals in the profile wings due to J-state interference and magneto-optical effects (Belluzzi & Trujillo Bueno 2012; Alsina Ballester et al. 2016; del Pino Alemán et al. 2016, 2020) only the line core is visible in prominences. Therefore our study focuses on the core of the Mg ii k line. This line is sensitive to both the Zeeman and Hanle effects. Its circular polarization degree due to the Zeeman effect scales linearly with $\mathcal{R} = 1.5 \times 10^{-4} B$ (see Eq. 1 of Trujillo Bueno & del Pino Alemán 2022), allowing for the determination of the line-of-sight (LOS) component of the magnetic field, $B_{\rm LOS}$, while the transversal component in the plane of sky (which scales with $\mathcal{R}^2$) would be very difficult (or impossible) to determine via the Zeeman effect at the expected magnetic field strengths. The linear polarization of the Mg ii k line arises dominantly from the scattering of anisotropic radiation and the Hanle effect. The critical Hanle field of the line is $B_{\rm H} \approx 22$ G (see Eq. 2 of Trujillo Bueno & del Pino Alemán 2022), i.e., suitable for quiescent prominence diagnostics. However, diagnosing magnetic fields becomes challenging when the field is not constant along the line of sight and when radiation transfer needs to be considered because the prominence plasma is optically thick ($\tau > 1$) and not in local thermodynamic equilibrium (LTE), i.e., in the so-called NLTE regime.

The main aim of this paper is to theoretically investigate the Stokes inversion problem of the Mg II k line in solar prominences, taking into account the effects of 3D radiative transfer. To this end, we use an optically thick 3D prominence model with a spatially varying magnetic field along the model's loop-like structure. Because the model's physical properties vary along the three spatial directions, we can have breaking of the axial symmetry of the incident radiation field at each point within the medium without the need of a magnetic field. Such non-magnetic causes of symmetry breaking can have an important impact on the linear polarization signals caused by the scattering of anisotropic radiation (e.g., Štěpán & Trujillo Bueno 2013; Jaume Bestard et al. 2021), which at the line center are sensitive to the presence of magnetic fields via the Hanle effect. In addition to anisotropic radiation pumping and the Hanle effect, our study also includes the Zeeman effect which dominates the line's circular polarization. Given that in prominences the Mg II k line does not show extended wings, where the effects of partial frequency redistribution and J-state interference are very important (Belluzzi & Trujillo Bueno 2012), in this investigation we solve the 3D NLTE radiative transfer problem assuming complete frequency redistribution without J-state interference. Our approach to the 3D Stokes spectral synthesis and inversion problem without assuming LTE can be found in Štěpán et al. (2022).

In this paper, we focus on investigating the suitability of the Mg II k line for spectropolarimetric diagnostics of optically thick prominences, which requires understanding the magnetic field's impact on the polarization of the emergent spectral line radiation. In particular, we ask if our 3D Stokes inversion, which consistently accounts for RT without assuming LTE, can uncover the global magnetic field geometry of an optically-thick prominence using the Mg II k line. Sect. 2 describes the prominence model and the spectral synthesis of the emergent Stokes profiles taking into account the effects of RT in the 3D model. In Sect. 3 we apply the Weak Field Approximation (WFA; see Sect. 9.6 in Landi Degl'Innocenti & Landolfi 2004), a Bayesian approach based on the constant-property slab model, and the full 3D Stokes inversion to the synthetic data, assessing the goodness of the inference. Finally, Sect. 4 outlines our conclusions.

2. Prominence model and synthesis of the Stokes profiles

Figure 1 illustrates the prominence model we have used to investigate the performance of the three inference methods we applied to the synthetic Stokes profiles. Although it is an academic prominence model with a relatively simple magnetic field geometry, it features the main ingredients that can affect the performance of the inversion, namely a non-trivial variation of the physical quantities both across the field of view (FOV) and along the line of sight (LOS), and a relatively large optical thickness to manifest the effects of RT in three-dimensional (3D) geometry.

For simplicity, we assume that all Mg atoms are in the Mg II ionization stage. At chromospheric temperatures the Mg II ion is indeed the dominant species (Leenaarts et al. 2013), and at about 15–20 kK the Mg II/Mg III fraction quickly decreases and Mg III becomes the dominant species (Heinzel et al. 2014). We model the Mg II k resonance line using a two-level atom model and in the limit of complete frequency redistribution. These two approximations can be justified because we can directly specify the total population in the lower and upper levels of the k line of Mg II (avoiding the need to account for an equation of state and for ionization and recombination processes) and because the line center, dubbed k_3, is not strongly affected by partial frequency redistribution effects (Leenaarts et al. 2013; Trujillo Bueno et al. 2017).[1] Finally, we assume an abundance of 7.544 for magnesium. Given the academic nature of our 3D prominence model, we assume that hydrogen, which is the most important donor of electrons under the considered thermodynamic conditions, is fully ionized. We can then estimate the electron volume density directly from the volume density of magnesium and its abundance. The inelastic collisional rates in the Mg II k line transition have been calculated using the data by Sigut & Pradhan (1995).

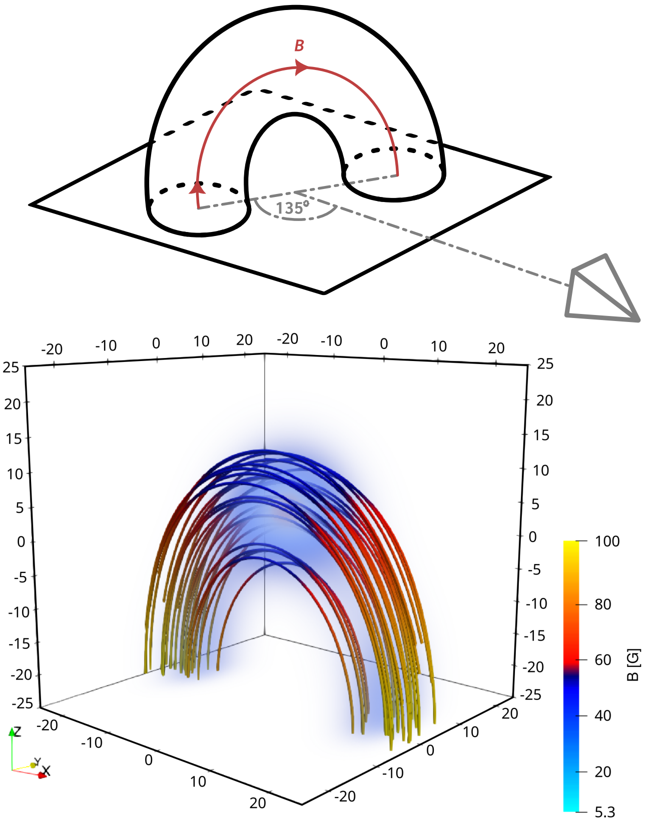

Fig. 1. Top panel: Line of sight of the observation. The symmetry plane of the prominence model is rotated by 45° with respect to the LOS. The red curve indicates the geometry of the magnetic field. Bottom panel: Visualization of the magnetic field lines in the $50 \times 50 \times 50\,\mathrm{Mm}^3$ spatial domain of the 3D prominence model.

The spatial domain of our prominence model is $50 \times 50 \times 50\ \mathrm{Mm}^3$, containing a loop-like structure whose legs start at the top of the chromosphere (the spatial domain sits on top of the C model of Fontenla et al. 1993, hereafter FAL-C model, at about 2.2 Mm above the visible solar surface) and extending up to about 40 Mm above it. The Mg II number density is prescribed and decreases outwards from the inner part of the prominence body. The optical thickness is maximum at the central part of the apex of the loop-like structure and exceeds 100 at the Mg II k line center. The prominence is isothermal, with a temperature of 10 kK, with a microturbulent velocity of 5 km/s (Heinzel et al.

---

[1] While strong velocity gradients can make the line center sensitive to PRD effects due to the Doppler shifts (Sukhorukov & Leenaarts 2017), the lack of bright wings in prominence profiles may diminish this effect.

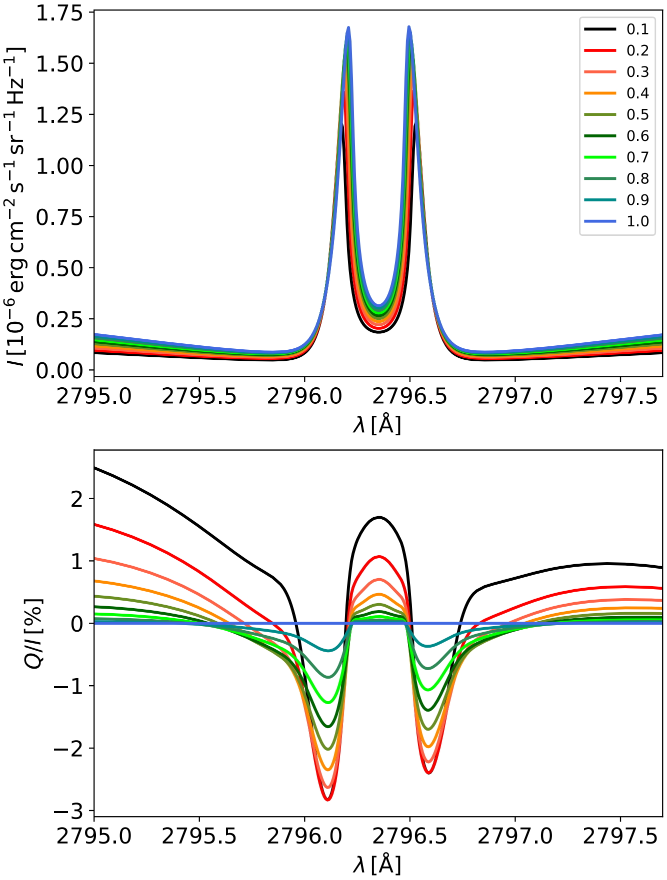

Fig. 2. The Stokes I and Q/I profiles of the emergent Mg ii k line radiation calculated in the FAL-C model atmosphere for various cosines (μ) of the heliocentric angle, from 0.1 to 1. The Stokes I and Q profiles are used for obtaining the illumination of the boundaries of the 3D prominence model.

2014). For simplicity, we do not include bulk velocities in this model. Finally, the magnetic field is such that the field lines follow the loop-like structure (see Fig. 1), with a strength reaching about 100 G close to the chromosphere and decreasing to about 40 G at the apex. These relatively strong magnetic fields have been chosen to produce a circular polarization signal above the considered noise level.

The prominence is illuminated by the underlying chromosphere, not limited to the computational domain. This illumination is axially symmetric and only depends on the angle between the propagation direction and the local vertical. The spectral profiles and their center-to-limb variation (see Fig. 2) have been calculated with HanleRT-TIC[2] (del Pino Alemán et al. 2016) using the FAL-C model. We note that in our solution we do not approximate the geometry of the solar chromosphere by an infinite plane but we take into account the curvature of the solar surface.

We solve the NLTE RT problem in 3D by applying the spectral synthesis mode of our code (Štěpán et al. 2022), obtaining the J^K_Q radiation field tensor components everywhere in the domain, and the emergent Stokes profiles for the chosen LOS (see Fig. 1). The resulting FOV is shown in Fig. 3. The linear polarization is due to the scattering of anisotropic radiation and the Hanle effect, while the circular polarization is caused by the Zeeman effect. For the application of inference methods in Sect. 3 we select two particular positions in the FOV, marked with black and orange dots in Fig. 3. The spectra corresponding to these two locations, after adding Gaussian polarimetric noise with $\sigma = 5\times10^{-11}$ erg s^{-1} cm^{-2} Hz^{-1} sr^{-1}, of the order of 5×10^{-4} of the line-center intensity, are shown in Fig. 4. The material behind the black dot LOS has an optical thickness at the line center of about 160, showing the typical self-reversal in its intensity profile, while the orange dot LOS has a more modest optical thickness of about 2.5 at the line center, showing no self-reversal. In Fig. 5 we show how $B_{\rm LOS}$ and the line center opacity change with the optical thickness at the line center, τ, along the LOS for these two selected positions.

3. Magnetic field inference

In this section, we apply three methods to infer the magnetic field in the prominence model described in Sect. 2. In Sects. 3.1 and 3.2 we apply two commonly used inference techniques, both of them based on strong assumptions for the RT. These two methods are applied pixel by pixel, and for the presentation of the results we have chosen two particular positions in the FOV (see black and orange dots in Fig. 3), which are representative of a LOS with significant optical thickness at the line center (> 100) and a LOS with a modest optical thickness at the line center (∼ 2.5). In Sect. 3.3 we apply our 3D Stokes inversion to infer the magnetic field vector in the whole prominence body and its surroundings. In particular, we are interested in assessing the goodness of the fits in the different methods and discussing their advantages and disadvantages.

3.1. Weak field approximation (WFA)

When the Zeeman splitting of the line's levels produced by the magnetic field is much smaller than the spectral line width, and under other certain assumptions, it is possible to find a closed and simple expression for the circular polarization, the so-called WFA (see, e.g., Sect. 9.6 of Landi Degl'Innocenti & Landolfi 2004),

$$V(\lambda) = -C\lambda_0^2 B_{\rm LOS} g_{\rm eff} \frac{\partial I}{\partial \lambda}(\lambda), \tag{1}$$

where $C = 4.6686\times10^{-13}$ G^{-1}Å^{-1}, λ_0 is the wavelength of the spectral line in Å, $g_{\rm eff}$ is the effective Landé factor (7/6 for the Mg ii k line), and $B_{\rm LOS}$ is the longitudinal component of the magnetic field in gauss.

The first assumption that must be fulfilled for the applicability of the WFA is that the Zeeman effect must be the only mechanism contributing to the polarization. While in solar prominences the linear polarization of the Mg ii k line is produced by the scattering of anisotropic radiation and the Hanle effect, the circular polarization is dominated by the Zeeman effect. Consequently, in this subsection, we focus only on the circular polarization profiles.

The second assumption for the applicability of the WFA is that $B_{\rm LOS}$ must be constant along the LOS. While this condition seems really restrictive and close to impossible to fulfill, in practice it means that $B_{\rm LOS}$ must be approximately constant along the LOS in those regions actually contributing to the emergent profiles. It is also clear from Eq. (1), which relates Stokes V and the derivative of the intensity I, that when the profiles are formed in extensive regions, the contributions to both Stokes parameters must come from the same regions along the LOS.

---

[2] The 1D NLTE code is publicly available at `https://gitlab.com/TdPA/hanlert-tic`.

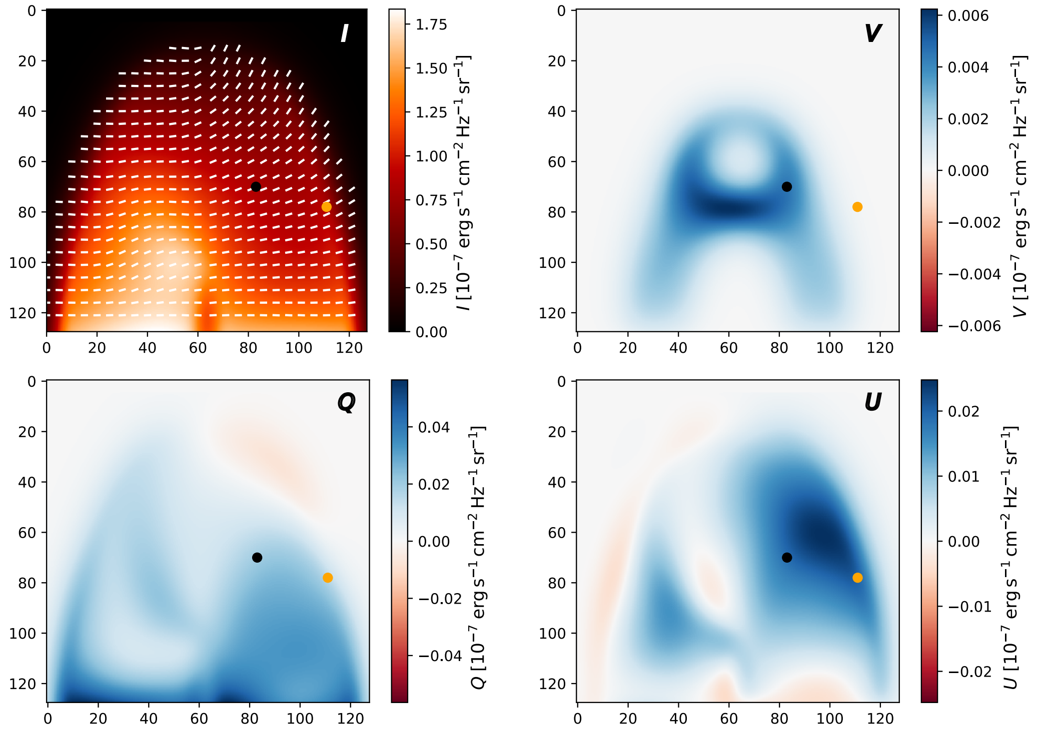

Fig. 3. Emergent radiation at each point in the 128 × 128 pixels field of view in the observation as illustrated in the top panel of Fig. 1. The I, Q, and U signals are shown at the line-center wavelength, while the V signal is shown at $\Delta\lambda = -0.079$ Å from the line center. The white vectors in the intensity panel show the orientation of the linear polarization at the line center. The black and orange dots indicate two particular locations in the FOV analyzed in the text.

If we assume uncorrelated and Gaussian noise, we can use Eq. (1) to calculate $B_{\rm LOS}$ as follows (Martínez González et al. 2012b),

$$B_{\rm LOS} = -\frac{1}{C}\frac{\sum_j V(\lambda_j) I'(\lambda_j)}{\sum_j (I'(\lambda_j))^2} \pm \frac{\sigma}{C\sqrt{\sum_j (I'(\lambda_j))^2}}, \tag{2}$$

where $I'(\lambda_j) = \lambda_0^2 g_{\rm eff} \frac{\partial I}{\partial \lambda}(\lambda_j)$, λ_j are the observed wavelengths, σ is the standard deviation of the Gaussian distribution of the noise in Stokes V, and the error is computed from the covariance matrix assuming a wavelength-independent standard deviation and a confidence level of 68.3 % (1σ).

In Fig. 6 we show the WFA fit to the Mg II k circular polarization profiles shown in Fig. 4, corresponding to the black and orange dots in Fig. 3, by applying Eq. (2). The fits are quite good and the corresponding $B_{\rm LOS}$ are -34.9 ± 2.3 and -36.6 ± 3.6 G for the black and orange dot profiles, respectively. From Fig. 5, we see that the retrieved $B_{\rm LOS}$ correspond approximately to the magnetic field around the maximum of the line-center opacity. Note that the τ scale in Fig. 5 corresponds to the line center wavelength and that the opacity quickly decreases for the line wings. Therefore, even if at the line core we cannot "see" the regions with $\tau \sim 80$ in Fig. 5, at the near wing wavelengths we can.

The WFA has the advantage of providing an estimation of $B_{\rm LOS}$ with negligible computing effort given that in our 3D model the required conditions are satisfied. However, the WFA returns a single number and an uncertainty that only accounts for the noise, thus there is no information about the magnetic field geometry and stratification, nor about other sources of uncertainty in the inferred values. For the particular cases we study in this work, it turns out that $B_{\rm LOS}$ is relatively constant along the formation region of the profiles, keeping the same polarity along the whole LOS, and thus the inferred $B_{\rm LOS}$ are rather good estimates. However, for more complex magnetic field geometries, with potential cancellation effects (different polarities along the LOS) or strong source function gradients, the WFA does not guarantee a good estimation of $B_{\rm LOS}$.

3.2. Constant-property slab Bayesian inversion

Most of the magnetic field inference in prominences (and filaments) over the last two decades relies on the modeling of spectropolarimetric observations in the He I triplet at 10830 Å and D_3 triplet at 5877 Å assuming a constant-property slab illuminated by the solar radiation of the underlying quiet Sun disk (see, e.g., the review by Trujillo Bueno & del Pino Alemán 2022, and references therein). Several inference methods based on this model can be found in the literature, such as look-up tables based on Principal Component Analysis (PCA; e.g., Casini et al. 2003), minimization methods such as that implemented in the Hanle and Zeeman Light (HAZEL) code (Asensio Ramos et al. 2008), or through Bayesian statistical approaches (e.g., Díaz Baso et al. 2019).

One of the main assumptions of this modeling approach is that the radiation pumping within the slab is fully dominated by the cylindrical symmetric illumination from the underlying solar disk (i.e., that the excitation of the atoms within the slab is not affected by RT within the slab). In order for this approximation to be reasonable, the optical thickness of the slab plasma should be small enough (Trujillo Bueno & Asensio Ramos 2007; Vicente Arévalo et al. 2023). The model then assumes that all properties of the plasma within the slab are constant along the LOS. Typically, a single slab is assumed in the modeling, but several components both side-by-side (e.g., Xu et al. 2010) or one after

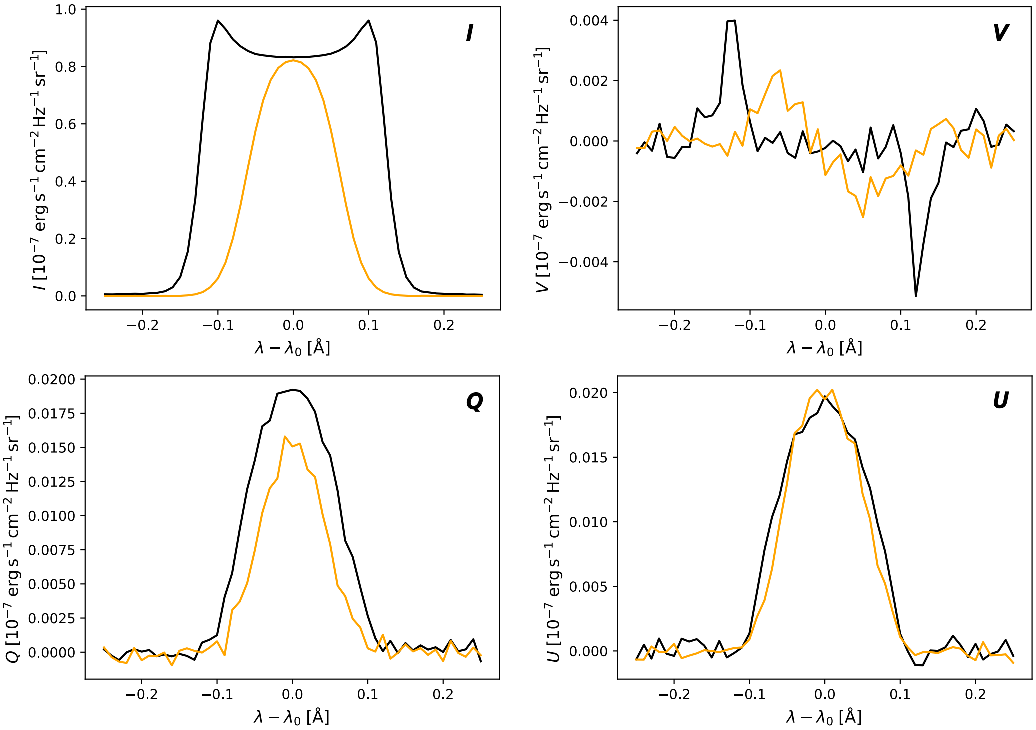

Fig. 4. Stokes profiles with an added Gaussian noise with $\sigma = 5 \times 10^{-11}$ erg s^{-1} cm^{-2} Hz^{-1} sr^{-1} at the points indicated by the black and orange dots in Fig. 3.

the other along the LOS (e.g., Martínez González et al. 2012a) have been considered.

When the modeling assumptions are satisfied, these inference methods can provide estimations of the magnetic field vector while allowing for the study of ambiguities and uncertainties. However, when the optical depth is of the order of, or larger than, the unity along any direction within the prominence (or filament), or if the plasma properties are not constant in the region along the LOS where the line forms, the accuracy of the inference can be severely compromised. Moreover, the inference methods based on Bayesian statistics, while providing a clear picture of the uncertainties and ambiguities, are computationally heavy, especially when considering more than a single slab.

In prominences, the Mg ii k line investigated in this work typically shows larger optical thickness than the He i triplet lines (Jejčič et al. 2018). Consequently, an unsuitable performance of the constant-property slab model is, a priori, expected. At the pixel marked with a black dot in Fig. 3 the plasma of our 3D model is very optically thick at the k-line center, with an optical depth of over one hundred. Its intensity profile (black curve in Fig. 4) shows a clear self-reversal, which cannot be reproduced assuming a single constant-property slab. On the contrary, at the orange dot pixel in Fig. 3 the plasma of our 3D model has a total optical depth of about 2.5 along the LOS. This pixel is near the prominence "edge" and it can thus "see" most of the underlying chromosphere. Note, however, that the prominence body blocks some of the chromospheric radiation, so the assumption of cylindrically symmetric illumination is not fully valid. The $B_{\rm LOS}$ is approximately constant along the LOS for the orange dot pixel (see bottom panel of Fig. 5), but the inclination of the magnetic field vector changes along the LOS.

We calculate the Bayesian posterior distribution for the case of a single-component constant-property slab model inversion of the emergent Stokes profiles at the location of the orange dot pixel. The parameters of our model are $B_{\rm LOS}$, the cosine of the polar angle of the magnetic field inclination with respect to the solar radius, μ_B, its azimuth in the plane normal to the radius with respect to the projection of the LOS on such plane, χ_B, the thermal width of the line, Δv_D, and the line-center optical thickness, τ. We use a Jeffreys prior[3] for τ and uniform priors for the rest of the parameters, between 0 and 1000 G for $B_{\rm LOS}$, between -1 and 1 for μ_B, between 0 and 2π for χ_B, and between 0.1 and 10 km/s for Δv_D.

Fig. 7 shows the marginalized posterior distributions for $B_{\rm LOS}$, μ_B, and χ_B. Although the physical properties of the 3D model at the selected pixel do not fulfill the applicability conditions, because the optical depth is larger than unity, the illumination is not cylindrically symmetric, and μ_B changes along the LOS, the inferred $B_{\rm LOS}$ turns out to be as good as with the WFA (see Sect. 3.1) and, moreover, the constant-property slab approach is capable of finding χ_B up to the ambiguities. This inversion method is much slower than the WFA, but in exchange it provides additional physical information.

Even though the $B_{\rm LOS}$ inference is rather good, the magnetic field strength is overestimated by about a factor of 2 (hence the magnetic field energy density by a factor of 4) due to the significant uncertainty in μ_B. Due to the symmetry assumed in the 3D model, there are ambiguous solutions for both μ_B and χ_B.

For an optically thin prominence with a not-too-complex magnetic field geometry, approaches based on this constant-property slab model (Bayesian inference, PCA, etc.) seem to be optimal since they can provide maximum information on uncertainties even when there are no self-consistent RT constraints.

---

[3] We have performed identical calculations using a uniform prior for τ and the results we have obtained are very similar. Nevertheless, our numerical experiment shows that the uniform prior for τ leads to slight overestimation of both τ and $B_{\rm LOS}$.

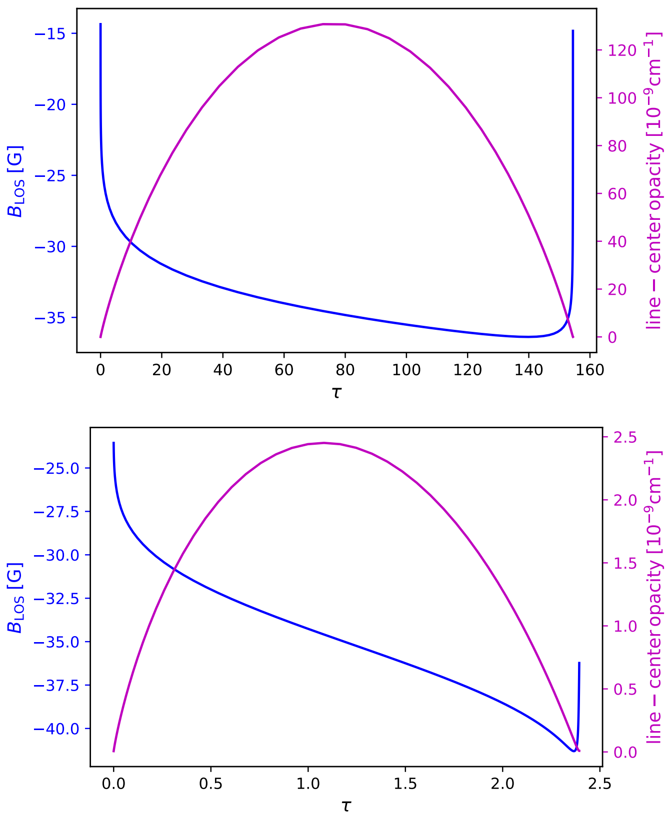

Fig. 5. Variation of the LOS component of the magnetic field (blue line) and of the line-center opacity (magenta line) at the black (top panel) and orange (bottom panel) spatial points indicated in Fig. 3. The horizontal axis gives the line-center optical depth along the LOS.

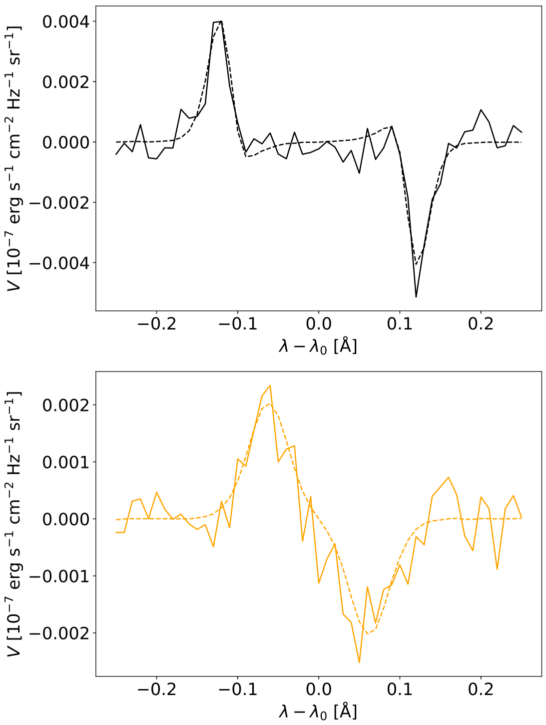

Fig. 6. The WFA best fits (dashed curves) of the spectra shown in Fig. 4 (solid curves). A noise level of $\sigma = 5 \times 10^{-11}$ erg s^{-1} cm^{-2} Hz^{-1} sr^{-1} corresponding to approximately to $6 \times 10^{-4} I_{\rm LC}$ has been added to the profiles, where $I_{\rm LC}$ is the line-center intensity. The inferred longitudinal components of the magnetic field are −34.9 ± 2.3 G for the top panel and −36.6 ± 3.6 G for the bottom panel.

3.3. 3D Stokes inversion

The third inference method we have applied to the synthetic Stokes profiles that we calculated by solving the NLTE RT problem in our 3D prominence model is the 3D Stokes inversion approach described in Štěpán et al. (2022). This method approaches the inverse problem by finding the physical quantities in the whole spatial domain of the 3D model simultaneously. Different regions of the model's spatial domain are coupled by the transfer of polarized radiation and, in addition, the solution can have additional constraints such as those from the magnetohydrodynamic equations. As described in detail in the aforementioned paper, this mesh-free method does not rely on calculating a sequence of self-consistent forward models leading to the minimum of a merit function. Instead, it follows an unconstrained minimization method in which unphysical solutions are allowed but penalized via regularization terms in the merit function. This allows obtaining relatively accurate solutions within a significantly smaller computing time. This method does not only provide a solenoidal magnetic field vector $\boldsymbol{B}$ everywhere in the model's spatial domain, but for our particular case also other thermodynamic quantities such as the atomic number density.

We have solved the inversion problem using 480 CPU cores of the OASA computer of the Astronomical Institute in Ondřejov. The solution shown here was reached in about 20 hours or 10^4 CPU hours. As mentioned above, we have penalized unphysical (non-self-consistent) solutions and magnetic field vector distributions not fulfilling $\nabla \cdot \boldsymbol{B} = 0$. The initial state of the magnetic field vector components has been chosen so that all the amplitudes of the basis functions were randomly sampled from a normal distribution with zero mean and a standard deviation of 20 G. The initial guess of the atomic number density has been a constant function equal to $\log_{10} N = 1$ in the units of $[N] = \mathrm{cm}^{-3}$.

In order to evaluate the goodness of the inversion we quantify the error in the inferred magnetic field with

$$e = \frac{||\boldsymbol{B}_{\rm inv} - \boldsymbol{B}||}{||\boldsymbol{B}||}\,, \tag{3}$$

where $\boldsymbol{B}$ is the true magnetic field vector (see Fig. 1) and $\boldsymbol{B}_{\rm inv}$ is magnetic field vector resulting for the inversion. Fig. 8 shows the histogram of this quantity evaluated at 10^5 randomly located points in the whole 3D domain (blue histogram) and with the same number of random points within the prominence body (orange histogram). As the Stokes parameters of the Mg II k line give us information about the "visible" surface of the prominence, whose size is comparable to that of the model's domain, the two histograms are relatively close.

We find a typical relative error in the inferred magnetic field vector of about 20–30 %. However, it is important to emphasize that using this relative error as a measure of the quality of the inference can be misleading. For instance, a small spatial displacement of a magnetic loop, e.g., at position $(X, Z) = (0, -25)$ Mm can lead to a very significant relative error. In Fig. 9 we show a cut in the X–Z plane of the original and inferred spatial distribution of the magnetic field vector and of the atomic number density, demonstrating that the inversion does a pretty good job in recovering the overall physical model.

Given the available CPU time, we have performed about two dozen inversions with different initializations of the model and different setups of the inversion algorithm. This is not enough to

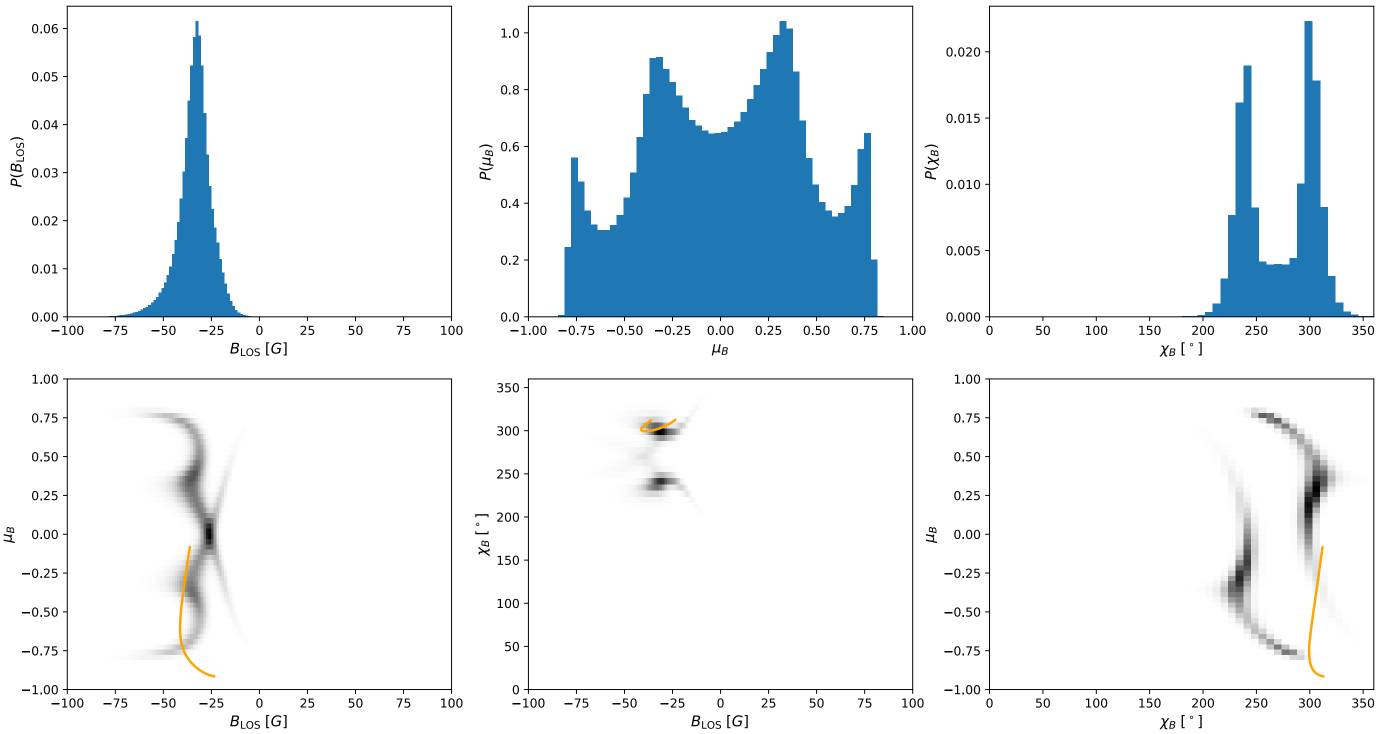

Fig. 7. Marginal posteriors of the Bayesian model parameters. The orange curves in the bottom panels indicate the variation of the actual parameters along the chosen LOS in the spatial domain of the original model. See text for details.

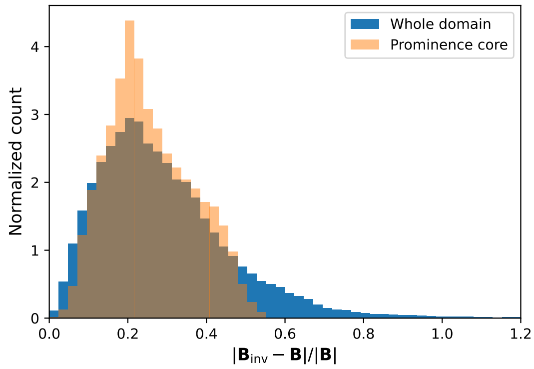

Fig. 8. Histogram of the errors (see Eq. 3) in the magnetic field inferred via the 3D Stokes inversion.

make any quantitative conclusions about the ability of different setups to perform the inversion. But overall, we have found that the model has either converged to a solution similar to the one presented in this section, ended up in a local minimum of the merit function, or has diverged. This last situation has occurred in cases where the inversion algorithm setup can be considered too aggressive (i.e., too large iteration steps, etc.). Importantly, the solution did never converge to any solution fundamentally different and ambiguous from the one presented here. This is indicative that, at least for this 3D academic prominence model, the global consistency imposes constraints strong enough to remove the ambiguities present in approaches assuming either no coupling between the FOV pixels or unrealistic symmetric conditions. Consequently, the non-trivial spatial coupling through RT seems to impose strong constraints on the solutions that are possible, leading to robust results.

Concerning the linear polarization signals caused by scattering processes, it is important to emphasize that they are sensitive mostly to regions not much deeper than optical depth unity along the LOS, where the anisotropy of the radiation can be substantial so as to produce observationally relevant linear polarization signals. Given that the Mg ii k line can be very optically thick in this prominence model, the inversion cannot be expected to perfectly recover the magnetic field in these optically inaccessible regions for which the Stokes profiles do not give us enough information. Nevertheless, the 3D inversion provides a sufficiently good estimate of the global structure and strength of the magnetic field.

4. Discussion and conclusions

We have solved the non-LTE problem of the generation and transfer of polarized radiation in the Mg ii k line in an academic 3D prominence model, where the magnetic field lines follow an optically thick loop-like structure. We have chosen this relatively simple geometry to facilitate the comparison between different magnetic field inference approaches. We have found that, despite 3D RT effects, for this relatively simple prominence model both the WFA and the constant-property slab approaches can give good estimations of the longitudinal component of the magnetic field from the observed Stokes *V* profile. To some degree, the constant-property slab approach is able to estimate the magnetic field transversal component from the linear polarization. In order to recover the full 3D picture, a full Stokes inversion method including the effects of RT in 3D is necessary, such as the one we have applied in this paper.

We have found that the WFA provides a fast estimation of $B_{\rm LOS}$ which is suitable at least for a simple structure such as our prominence model. For profiles with small enough optical thickness along the LOS, methods based on the constant-property slab model seem to be the best approach in terms of recovered in-

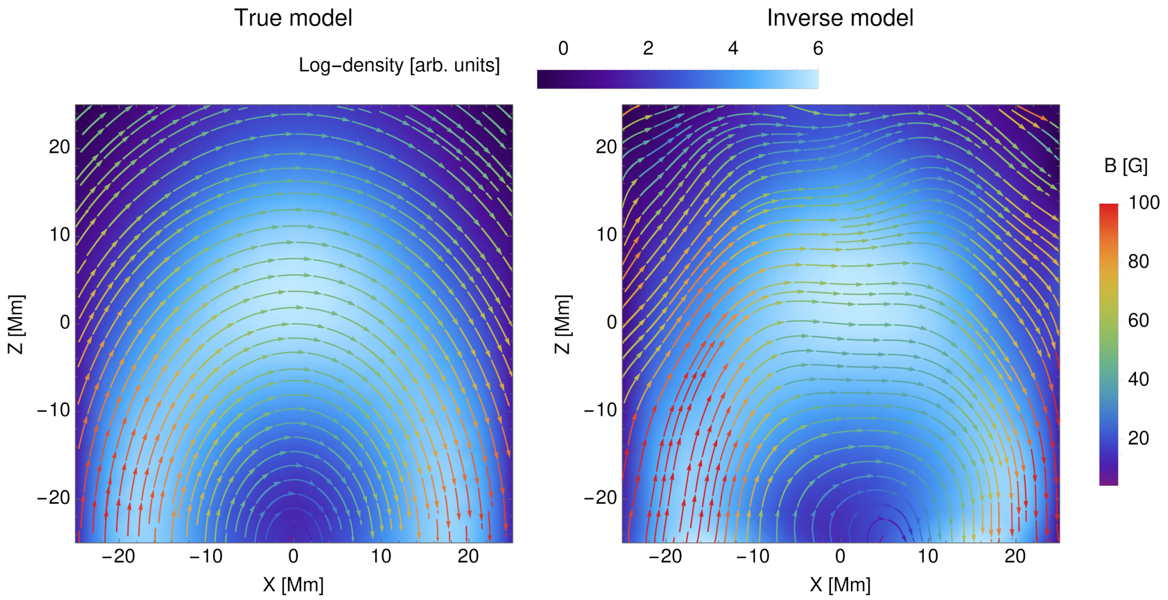

Fig. 9. Comparison of vertical slices through the $Y = 0\,\mathrm{Mm}$ plane in the original model and in the model resulting from the 3D inversion. The left panel shows the magnetic field lines and the density in the original model, while the right panel shows the same quantities in the inferred model. The background color in both panels represents the log-density of Mg II ions. Our 3D Stokes inversion successfully captures the essential morphology of the original model.

formation and computational time required, if the prominence shows a simple enough geometry. When the optical thickness exceeds unity we can take advantage of the RT coupling by applying our full 3D RT approach and inferring the global structure of the prominence.

Due to the significant optical thickness in our 3D model, also found in actual prominences (e.g., Jejčič et al. 2018), the Stokes Q and U profiles are mostly sensitive to the outermost layers of the prominence (in the direction toward the observer). This is more critical in prominences because, unlike on-disk observations, the wings are not observed. In contrast with the He I lines more popularly used in prominence diagnostics, the Mg II k line is a strong resonance line with spectral structure. This entails that the chromospheric radiation illuminating the prominence plasma is sensitive to velocities, introducing frequency shifts between the absorption profile and the incoming illumination spectrum, and to variations in the chromospheric surface producing significant changes in the intensity of this line.

The significant optical thickness can be even more problematic if the real physical scenario is that of many small-scale threads with their own prominence-corona transition regions (e.g., Gunár et al. 2007). In this case, the inversion can become extremely challenging. Therefore, spectral lines with smaller optical thickness in prominences, providing more spatially averaged information on the magnetic field, may provide very valuable additional information.

The scientific importance of developing a space telescope for making possible routine spectropolarimetric observations in the near-UV region of the Mg II h and k lines can hardly be overestimated, because the polarization signals that the combined action of scattering processes and the Hanle and Zeeman effects introduce in this spectral region encode a wealth of information on the magnetism and geometry of chromospheric and prominence plasmas. Equally important is the development of advanced plasma diagnostic techniques capable of providing reliable information on the magnetic field vector.

Acknowledgements. J.Š. acknowledges the financial support from project RVO:67985815 of the Astronomical Institute of the Czech Academy of Sciences. T.P.A.'s participation in the publication is part of Project RYC2021-034006-I, funded by MICIN/AEI/10.13039/501100011033, and the European Union "NextGenerationEU"RTRP. T.P.A. and J.T.B. acknowledge support from the Agencia Estatal de Investigación del Ministerio de Ciencia, Innovación y Universidades (MCIU/AEI) under grant "Polarimetric Inference of Magnetic Fields" and the European Regional Development Fund (ERDF) with reference PID2022-136563NB-I00/10.13039/501100011033.

References

Alsina Ballester, E., Belluzzi, L., & Trujillo Bueno, J. 2016, ApJ, 831, L15
Asensio Ramos, A., Trujillo Bueno, J., & Landi Degl'Innocenti, E. 2008, ApJ, 683, 542
Belluzzi, L. & Trujillo Bueno, J. 2012, ApJ, 750, L11
Bryans, P. & The CMEx Team. 2023, in American Astronomical Society Meeting Abstracts, Vol. 55, American Astronomical Society Meeting Abstracts, 214.02
Casini, R., López Ariste, A., Tomczyk, S., & Lites, B. W. 2003, ApJ, 598, L67
De Pontieu, B., Title, A. M., Lemen, J. R., et al. 2014, Sol. Phys., 289, 2733
del Pino Alemán, T., Casini, R., & Manso Sainz, R. 2016, ApJ, 830, L24
del Pino Alemán, T., Trujillo Bueno, J., Casini, R., & Manso Sainz, R. 2020, ApJ, 891, 91
Díaz Baso, C. J., Martínez González, M. J., & Asensio Ramos, A. 2019, A&A, 625, A128
Fontenla, J. M., Avrett, E. H., & Loeser, R. 1993, ApJ, 406, 319
Gunár, S., Heinzel, P., Schmieder, B., Schwartz, P., & Anzer, U. 2007, A&A, 472, 929
Heinzel, P., Vial, J. C., & Anzer, U. 2014, A&A, 564, A132
Hillier, A. 2018, Reviews of Modern Plasma Physics, 2, 1
Jaume Bestard, J., Trujillo Bueno, J., Štěpán, J., & del Pino Alemán, T. 2021, ApJ, 909, 183
Jejčič, S., Schwartz, P., Heinzel, P., Zapiór, M., & Gunár, S. 2018, A&A, 618, A88
Landi Degl'Innocenti, E. & Landolfi, M. 2004, Polarization in Spectral Lines, Vol. 307 (Kluwer Academic Publishers)
Leenaarts, J., Pereira, T. M. D., Carlsson, M., Uitenbroek, H., & De Pontieu, B. 2013, ApJ, 772, 89
Martínez González, M. J., Asensio Ramos, A., Manso Sainz, R., Beck, C., & Belluzzi, L. 2012a, ApJ, 759, 16
Martínez González, M. J., Manso Sainz, R., Asensio Ramos, A., & Belluzzi, L. 2012b, MNRAS, 419, 153

McKenzie, D., Ishikawa, R., Trujillo Bueno, J., et al. 2021, in AGU Fall Meeting Abstracts, Vol. 2021, SH52A–06
Narukage, N., McKenzie, D. E., Ishikawa, R., et al. 2016, in Society of Photo-Optical Instrumentation Engineers (SPIE) Conference Series, Vol. 9905, Space Telescopes and Instrumentation 2016: Ultraviolet to Gamma Ray, ed. J.-W. A. den Herder, T. Takahashi, & M. Bautz, 990508
Paletou, F., Vial, J. C., & Auer, L. H. 1993, A&A, 274, 571
Sigut, T. A. A. & Pradhan, A. K. 1995, Journal of Physics B Atomic Molecular Physics, 28, 4879
Sukhorukov, A. V. & Leenaarts, J. 2017, A&A, 597, A46
Trujillo Bueno, J. & Asensio Ramos, A. 2007, ApJ, 655, 642
Trujillo Bueno, J. & del Pino Alemán, T. 2022, ARA&A, 60, 415
Trujillo Bueno, J., Landi Degl'Innocenti, E., & Belluzzi, L. 2017, Space Sci. Rev., 210, 183
Vial, J. C. 1982, ApJ, 254, 780
Vicente Arévalo, A., Štěpán, J., del Pino Alemán, T., & Martínez González, M. J. 2023, A&A, 675, A45
Štěpán, J., del Pino Alemán, T., & Trujillo Bueno, J. 2022, A&A, 659, A137
Štěpán, J. & Trujillo Bueno, J. 2013, A&A, 557, A143
Xu, Z., Lagg, A., & Solanki, S. K. 2010, A&A, 520, A77